ARTICLE OPEN

Check for updates

Moiré straintronics: a universal platform for reconfigurable quantum materials

M. Kögl [1,3✉], P. Soubelet [2,3✉], M. Brotons-Gisbert [1], A. V. Stier [2], B. D. Gerardot [1] and J. J. Finley[2]

Large-scale two-dimensional (2D) moiré superlattices are driving a revolution in designer quantum materials. The electronic interactions in these superlattices, strongly dependent on the periodicity and symmetry of the moiré pattern, critically determine the emergent properties and phase diagrams. To date, the relative twist angle between two layers has been the primary tuning parameter for a given choice of constituent crystals. Here, we establish strain as a powerful mechanism to in situ modify the moiré periodicity and symmetry. We develop an analytically exact mathematical description for the moiré lattice under arbitrary in-plane heterostrain acting on any bilayer structure. We demonstrate the ability to fine-tune the moiré lattice near critical points, such as the magic angle in bilayer graphene, or fully reconfigure the moiré lattice symmetry beyond that imposed by the unstrained constituent crystals. Due to this unprecedented simultaneous control over the strength of electronic interactions and lattice symmetry, 2D heterostrain provides a powerful platform to engineer, tune, and probe strongly correlated moiré materials.

INTRODUCTION

Strong correlations among electrons arise when their mutual Coulomb interaction is similar or larger than their kinetic energy, and the delicate balance between these two energy scales determines the ground state of the system and its low-energy excitations. The rise of long period moiré patterns, formed by vertically stacking two atomically thin crystals with a lattice mismatch (δ) and/or relative twist angle (θ), provides a unique capability to tune the two critical energy scales (Coulomb interaction and kinetic energies)—and the electron density—over several orders of magnitude, creating a highly versatile solid-state quantum material platform[1]. The potential to engineer and probe strongly correlated states has been highlighted in several moiré material systems, including twisted bilayer graphene heterostructures near the magic angle[2–4] and homo-[5–7] or heterobilayer[8–11] transition metal dichalcogenide (TMD) moiré heterostructures. The physics of these systems is determined by the strong electronic interactions in the landscape defined by the underlying moiré potentials. Further examples of synthetic moiré materials in which new physical properties arise due to interlayer hybridization can be found in moiré trapped excitons[12,13], twisted 2D magnets[14–16], moiré solitons[17,18], moiré polaritons[19], and ferroelectric moiré materials[20–22].

The simplest model to understand strongly interacting quantum systems is the Hubbard model, which consists of a kinetic term defined by the hopping parameter t and the on-site Coulomb repulsion U. In the Hubbard picture, when $U/t > 1$ the kinetic energy is quenched, and strong electronic correlations emerge. Although it is expected that the Hubbard model can provide valuable insight into phenomena such as high-temperature superconductivity or exotic magnetic states[23,24], only the one-dimensional (1D) case can readily be solved. The solution to higher dimensional problems depends on a delicate balance between the different model parameters and the lattice geometry[1]. Hence, quantum simulators based on ultracold atomic optical

lattices, where it is possible to preset the lattice geometry and tune U/t by adjusting the laser power and U using Feshbach resonance techniques[25], have become an exciting avenue to probe the Hubbard model and explore emerging quantum materials[26].

Although 2D moiré materials offer access to different energy scales and a broader range of density and temperature than what is achievable in cold atom optical lattices, the same wide-ranging in situ tunability (of lattice symmetry, U, and t) possible in optical lattices has proven to be elusive for 2D quantum materials. While the interlayer coupling and band alignment can be tuned in situ by displacement fields[5,6,22], U and t can only be tuned via the choice of constituent materials, the stacking angle θ or adjusting the dielectric environment of the active moiré region[27,28]. Since θ and the permittivity of the surrounding layers are set during the fabrication of the moiré heterostructure, direct continuous modification of the Hubbard model parameters is not readily achievable[29], restricting the capability to fine-tune parameters near critical points and broadly explore phase diagrams. This limitation constrains the usefulness of moiré materials as quantum simulators.

The effect of heterostrain[30,31] in homo- and heterostructures, i.e., the presence of a differential strain between the layers that compose the structure, was found as a path forward to tailor their electronic properties. The heterostrain issue was extensively studied from the theoretical point of view[30,32–35] with the aim to, for instance, design flat bands in bilayer graphene and TMD structures[32,34]. From the experimental side, heterostrain was mainly studied in unintentionally strained structures or systems without in situ tuning[31,36–38] and only a few experimental realizations have focused on the implementation of devices to intentionally apply heterostrain on demand[17,39]. However, the use of heterostrain to directly affect the moiré superlattice with the perspective to tune U/t has not been fully investigated. In this work, we explore the effect of heterostrain on the size and

geometry of moiré lattices formed in vertically stacked bilayers of van der Waals materials. Using a generic analytical approach that is independent of the intrinsic crystal structure, we describe the effects of biaxial, uniaxial, and shear heterostrains for realistic experimental conditions. We find that depending on the type of strain, we can tune the moiré wavelength or even smoothly modify the moiré lattice from, e.g., triangular into rectangular lattices. Furthermore, the moiré wavelength can be tuned in situ in different lattice directions to break symmetries in the system, satisfying lattice conditions required for exotic quantum models beyond the standard Hubbard model, such as coupled Luttinger chains[40]. Finally, we show that the use of heterostrain can be implemented to fine-tune and tailor structures to overcome fabrication variabilities that are typically present, for instance, in magic-angle graphene and other moiré materials[41]. We thus show that strain control is a promising strategy to provide the critical degree of freedom required to realize reconfigurable quantum materials and achieve a fully tunable on-chip quantum simulator.

RESULTS AND DISCUSSION

Mathematical description

Moiré lattices are large-scale interference patterns formed when the unit cells of adjacent layers deviate either by a small twist angle θ or a lattice constant mismatch δ[42]. In this work, we assume that the unit cell of both layers of the homo-/heterostructure are of similar geometry, while the size of the unit cell of one layer may deviate by a scaling factor $(1 + \delta)$. The following formulation describes a pure geometrical deformation of moiré lattices under a global 2D strain tensor in which each layer is considered as a rigid object, i.e., atomic reconstruction effects can be neglected. However, to reach an experimental realization, it is important to take atomic reconstruction into account. Possible experimental implementations are presented in Supplementary Note 5. In structures with small stacking angles, atoms within each layer try to adjust the stacking landscape forming commensurate regions[17,43–45]. This effect increases interlayer adhesion and leads to higher friction between layers that hinders the possibility of modifying the atomic registry[29,46,47]. Conversely, higher stacking angles reduce the reconstruction effects and avoid strain transfer between layers ($\mu \neq 0$). For MoSe$_2$-WSe$_2$ heterostructures, these critical angles are found to be 2.5° and ~1.0° for 3R and 2H stacking, respectively[44,48,49], and increase to ~3.0° in the case of 2H homobilayers[45]. Hence, it is possible to avoid atomic reconstruction by using a stacking angle above the critical angle of the bilayer. On the other hand, while the atomic reconstruction is always present, heterostrain can also reduce interlayer interaction and prevents atomic reconstruction[50], as it has been shown that $\epsilon_u \sim 3\%$ can transform a totally commensurate moiré lattice ($\theta = 0°$) into a partially incommensurate structure with reduced atomic reconstruction[17].

The most general moiré pattern is formed between two monoclinic lattices with Bravais lattice vectors $\mathbf{a}_i$ for the *lower* layer and $\mathbf{b}_i$ for the *upper* one, as sketched in Fig. 1a. These primitive lattice vectors can be written as follows:

$$\mathbf{a}_i = a_i R_{\psi_i} \cdot \begin{pmatrix} 1 \\ 0 \end{pmatrix}$$
$$\mathbf{b}_i = a_i(1 + \delta) R_{\psi_i + \theta} \cdot \begin{pmatrix} 1 \\ 0 \end{pmatrix}, \quad (1)$$

where a_i are the lattice constants of a general 2D monoclinic lattice and R_{ψ_i} is the 2D rotation matrix with an angle ψ_i. The angle ψ_i is

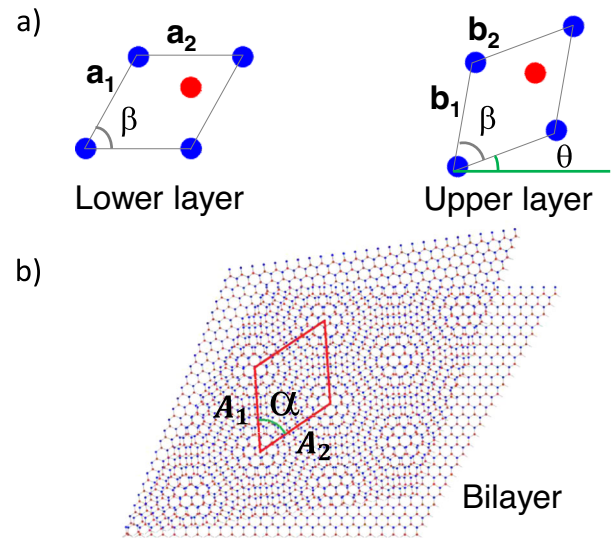$$\psi_i = \begin{cases} \theta_0 \, ; \, i = 1 \\ \theta_0 + \beta \, ; \, i = 2 \end{cases} \quad (2)$$

Fig. 1 Relevant parameters describing the moiré lattice formed by monolayers of hexagonal crystals, such as graphene and TMDs. a Sketch of the different TMD layers that compose the moiré lattice. The lattice parameters of the first (second) layer are $\mathbf{a}_1$ ($\mathbf{b}_1$) and $\mathbf{a}_2$ ($\mathbf{b}_2$), the angle between those vectors is β for both layers, and the relative angle between the lattices is θ. **b** Moiré lattice parameters A_1 and A_2 and the internal angle α between those vectors in a bilayer formed by the hexagonal monolayer crystals.

with θ_0 being the overall rotation of the lattices compared to the x-axis and β the angle between the primitive lattice vectors $\mathbf{a}_1(\mathbf{b}_1)$ and $\mathbf{a}_2(\mathbf{b}_2)$. The stacking of these TMDs results in a bilayer system with a moiré pattern as presented in Fig. 1b. Such a lattice is characterized by the moiré lattice vectors $\mathbf{A}_1$ and $\mathbf{A}_2$ whose magnitudes are A_1 and A_2, respectively. In addition, we define as α the angle between those vectors.

In the next step, both lattices are subject to a geometric deformation due to an applied strain on the bottom layer, expressed by a general 2D strain tensor ϵ. We restrict our discussion to a global strain that is uniform across the whole layer. To account for any slippage between layers, we introduce the strain transfer parameter μ. This strain transforms the Bravais lattice vectors $\mathbf{a}_i$ and $\mathbf{b}_i$ of the individual layers in the form

$$\mathbf{a}'_i = a_i(\mathbb{I} + \epsilon) \cdot R_{\psi_i} \cdot \begin{pmatrix} 1 \\ 0 \end{pmatrix}$$
$$\mathbf{b}'_i = a_i(1 + \delta)(\mathbb{I} + \mu\epsilon) \cdot R_{\psi_i + \theta} \cdot \begin{pmatrix} 1 \\ 0 \end{pmatrix}. \quad (3)$$

The parameter μ allows us to model different experimental setups (see Supplementary Note 6), for instance, a system where the lower layer is clamped directly to the substrate while the upper one is only in contact with the first one. Since the interlayer friction is high for commensurate structures (small θ or δ) and low for incommensurate structures (high θ or δ), the transferred strain in the second layer is different for each case[29,46,47]. In the incommensurate case, the strain on the lower layer is not transferred to the upper one, i.e., $\mu = 0$, which we refer to as heterostrain. For small θ or δ, the layers are more commensurate such that $0 < \mu < 1$. A full transfer of strain $\mu = 1$ is referred to as homostrain.

The strain tensor ϵ is commonly written as a symmetric 2×2 matrix with three independent parameters[32]. Hence, we express the strain matrix as follows:

$$\epsilon = \begin{pmatrix} \epsilon_{xx} & \epsilon_{xy} \\ \epsilon_{xy} & \epsilon_{yy} \end{pmatrix} = \epsilon_c \mathbb{I} + \epsilon_s S_{\phi_s}, \quad (4)$$

where we define

- $\epsilon_c = \frac{\epsilon_{xx} + \epsilon_{yy}}{2}$ as biaxial strain,

- $\epsilon_s = \sqrt{\left(\frac{\epsilon_{xx} - \epsilon_{yy}}{2}\right)^2 + \epsilon_{xy}^2}$ as shear strain,

- $S_{\phi_s} = \cos(\phi_s)\sigma_x + \sin(\phi_s)\sigma_z$ as shear matrix, and

- $\phi_s = \arccos\left(\frac{\epsilon_{xy}}{\epsilon_s}\right)$ as shear strain angle.

Our strain parameterization follows ref. [36], which separates the strain into biaxial strain ϵ_c (which changes the size of the unit cell) and shear strain ϵ_s (which alters the shape of the unit cell). Details on the physical meaning of the shear angle and different experimental feasibilities can be found in Supplementary Note 5. In this context, uniaxial strain ($\epsilon_{xx} = \epsilon_u$, $\epsilon_{xy} = 0$, $\epsilon_{yy} = -\nu\epsilon_u$) is a mixture of biaxial and shear strain with a shear angle set to $\phi_s = 90°$. Note that under uniaxial strain, the crystal is elongated along one direction, while in the perpendicular direction, the crystal deforms proportional to the Poisson ratio $-\nu$.

Using the previous definitions, it is possible to calculate the real space moiré lattice under general strain, as presented in Supplementary Note 1. The new moiré lattice vectors $\mathbf{A}'_i$ take the form

$$
\mathbf{A}'_i = \frac{a_i(1+\delta)}{\Delta}
$$
$$
\cdot \left[(1+\delta)c_\mu\left((1+\epsilon_c)\mathbb{I} + \epsilon_s S_{\phi_s}\right) \right.
$$
$$
\left. - c_1\left((1+\mu\epsilon_c)R_\theta + \mu\epsilon_s S_{\phi_s+\theta}\right) \right] \cdot R_{\psi_i} \cdot \begin{pmatrix} 1 \\ 0 \end{pmatrix}
\tag{5}
$$

where the denominator Δ is the expression

$$
\Delta = c_\mu(1+\delta)^2 + c_1
$$
$$
- 2(1+\delta)\left[(1+\epsilon_c + \mu\epsilon_c) + \mu(\epsilon_c^2 - \epsilon_s^2)\right]\cos(\theta),
\tag{6}
$$

$c_1 = (1+\epsilon_c)^2 - \epsilon_s^2$, and $c_\mu = (1+\mu\epsilon_c)^2 - \mu^2\epsilon_s^2$. Finally, we calculate the moiré unit cell area M as follows:

$$
M = \|\mathbf{A}'_1 \times \mathbf{A}'_2\| = a_1 a_2 \|\sin(\beta)\|\frac{(1+\delta)^2}{\|\Delta\|}c_1 c_\mu.
\tag{7}
$$

The full calculation is provided in Supplementary Note 2.

We emphasize that all manifestations of 2D strain are covered by these calculations and no approximations are made, in contrast to previous descriptions that focus on hexagonal lattices only and use approximations that only apply to specific strain configurations[30,32,33]. Note that expression (5) defines the moiré lattice vectors and can be employed for any homo- and heterobilayer structure with a similarly shaped unit cell.

In the particular case of homostrain, expression (5) leads to $\mathbf{A}'_i = (\mathbb{I} + \epsilon) \cdot \mathbf{A}_i$ which means that the strain is applied to the moiré vectors as if the moiré lattice is strained itself. Even though 2D materials can withstand very high strain levels[51], the maximum applicable strain is $\epsilon_c, \epsilon_s \ll 1$. Hence, the homostrain effect on the moiré lattice is very small and can be neglected in comparison to the effect of tuning the twist angle θ. However, in the case of imperfect strain transduction between the layers ($\mu < 1$) we find that strain has a substantial effect on the moiré size and shape, since the magnitude of the moiré vectors is dominated by the denominator Δ in expression (5). For example, in the homobilayer case, increasing biaxial strain ϵ_c decreases the moiré lattice parameters with the approximate dependence of $A'_i \propto 1/\|\epsilon_c\|$. In the context of the Hubbard model, the hopping parameter t decreases exponentially with A'_i while U scales inversely with A'_i[27,28] and, therefore, the ratio U/t can be modified by tuning ϵ_c. In contrast to θ, in situ strain tuning is experimentally viable, which allows direct tuning of U/t (see Supplementary Note 5).

In contrast to biaxial strain, shear strain can make the denominator Δ identically zero, leading to the divergence of the moiré vectors. This condition, referred to as a 1D moiré pattern[33],

has already been experimentally observed[52]. This effect occurs when the deformation of one layer due to shear strain aligns the lattice sites in one direction while leaving a mismatch in the perpendicular direction. We emphasize that this effect is not dependent on the orientation of the lattice θ_0, the shear angle ϕ_s or the shape of the layer lattices.

In addition to the size of the moiré pattern, shear strain is also able to change the moiré lattice geometry since ϵ_s changes the shape of the individual lattice depending on the orientation of ϕ_s and θ_0. The main defining parameter for the geometry of the moiré pattern is the angle α between the moiré vectors (see Fig. 1b). This angle takes the form

$$
\sin(\alpha) = \left\| \frac{\mathbf{A}'_1 \times \mathbf{A}'_2}{A'_1 A'_2} \right\|.
\tag{8}
$$

In the case of zero shear strain ($\epsilon_s = 0$), it can be shown that $\frac{a_1}{a_2} \overset{\epsilon_s=0}{=} \frac{A'_1}{A'_2}$ and that $\alpha \overset{\epsilon_s=0}{=} \beta$, proving that the shape of the moiré lattice is equal to the shape of the underlying lattice defined by $\mathbf{a}_i$, as presented in detail in Supplementary Note 3.

In contrast to in situ tuning of θ[53–55], 2D strain has the potential to tune the size and shape of the moiré pattern via the three independent strain parameters ϵ_c, ϵ_s and ϕ_s. In the following section, we will focus on the case of pure heterostrain ($\mu = 0$) on homo- and heterobilayer structures and show how the different types of strain can affect the moiré lattice geometry.

Biaxial heterostrain on hexagonal homo- and heterobilayers
In this section, we center our analysis on moiré patterns generated by monolayers with hexagonal lattices; in particular, we take WSe$_2$ homobilayers and MoSe$_2$-WSe$_2$ heterobilayers as paradigmatic cases. The lattice parameters used to perform the calculations are $a_{\text{MoSe}_2} = 0.329$ nm for MoSe$_2$[56] and 0.4% smaller for the WSe$_2$[56–58]. As shown in Supplementary Note 6, strategies can be proposed to avoid strain transfer for most bilayer structures. In the following, we analyze the pure heterostrain case, in which the deformation is applied to the lower layer, which, in our specific heterobilayer example, corresponds to the WSe$_2$ monolayer. The Poisson ratios are $\nu_{\text{MoSe}_2} = 0.23$ and $\nu_{\text{WSe}_2} = 0.19$ for MoSe$_2$ and WSe$_2$, respectively[56].

Figure 2a shows a sketch of the bilayer formation in which ϵ_c produces an in-plane elongation/contraction of the lower layer unit cell and the upper layer is stacked at an angle θ. The effect of ϵ_c and θ on the moiré pattern is depicted in Fig. 2b for homobilayer (left) and heterobilayer (right) structures. The vertical lines at $\epsilon_c = 0$ correspond to the well-known behavior of homo- and heterobilayers described in ref. [59], i.e., in the homobilayer case, the structure presents a divergence of A'_1 and A'_2 at $\theta = 0$ that evidences the absence of moiré patterns in naturally stacked bilayers (2H and 3R stacking order). However, the stacking of layers with $\theta \neq 0$ and/or $\epsilon_c \neq 0$ gives rise to moiré patterns whose periodicity (A'_1 and A'_2) decreases by increasing ϵ_c and/or θ. In the heterobilayer case, as the lattice parameter of WSe$_2$ is ~0.4% smaller than MoSe$_2$, the stretching of the WSe$_2$ layer by ~0.4% recovers the divergence observed at the point $\epsilon_c = 0$, $\theta = 0$ for homobilayers. Therefore the use of biaxial heterostrain in heterobilayers enables the formation of arbitrarily large moiré lattices as observed in homobilayer structures. Another important point to note is that due to the hexagonal symmetry of each layer, neither ϵ_c nor θ can modify the moiré lattice geometry that is also hexagonal, i.e., $A'_1 = A'_2$ and $\alpha = 60°$, as demonstrated in Supplementary Note 3. Consequently, different combinations of strain and stacking angle can lead to the same moiré lattice (but with a relative rotation). For instance, the dotted lines in both panels of Fig. 2b describe a unique moiré lattice with $A'_1 = A'_2 = 10$ nm. Supplementary Note 4 provides details regarding the direction
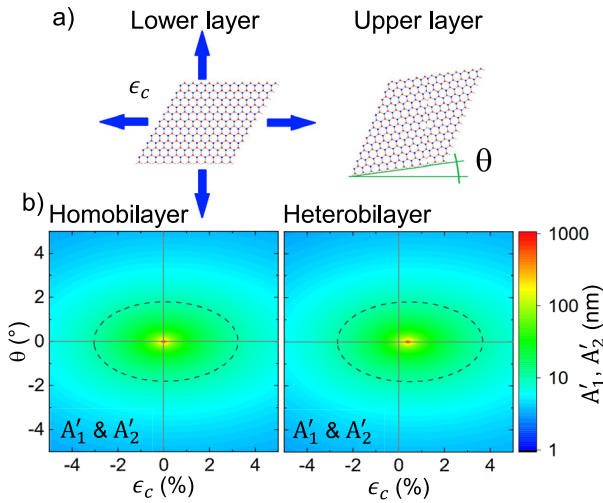
Fig. 2 Moiré lattice deformation in hexagonal bilayers under biaxial heterostrain. a Sketch of the moiré lattice formation. To perform the calculations, the biaxial strain ϵ_c, indicated through blue arrows, is applied to the lower layer. The upper layer is stacked with an angle θ respect to the lower one. **b** Moiré lattice parameters A'_1 and A'_2 as function of biaxial strain and stacking angle for homo- (left) and heterobilayer (right) structures.

of the moiré lattice with respect to the underlying lattice in the absence of shear strain.

Uniaxial heterostrain on hexagonal homo- and heterobilayers

We continue by describing the effect of uniaxial heterostrain on the moiré lattice generated in homo- and heterobilayers using the same material parameters as in the previous section. Figure 3a shows a sketch of this situation in which the lower layer is stretched/contracted along the zigzag direction by applying a uniaxial strain ϵ_u. Due to the Poisson effect, the direction perpendicular to ϵ_u is deformed by $-\nu\epsilon_u$, where ν is the Poisson ratio. In the case where the layer is stretched in the zigzag direction, the armchair direction is contracted (stretched) if $\nu > 0$ ($\nu < 0$). The upper layer is stacked at an angle θ with respect to the lower layer. Figure 3b depicts the moiré lattice parameters A'_1 (upper panels) and A'_2 (lower panels) for homobilayer- and heterobilayer structures (left and right panels, respectively). Uniaxial strain has a stronger influence on the moiré lattice than biaxial strain: (i) For uniaxial strain, the moiré lattice parameters A'_1 and A'_2 diverge along curves in the $\theta - \epsilon_u$ space instead of a single point (see red curves in Fig. 3b). (ii) ϵ_u breaks the degeneracy between A'_1 and A'_2. (iii) In heterobilayers, uniaxial strain cannot retrieve the moiré lattice geometry found in homobilayers.

In homobilayers, A'_1 and A'_2 diverge along lines that intersect at the origin ($\epsilon_u = 0$, $\theta = 0$). For heterobilayers, these curves do not intersect but show an avoided crossing behavior instead with vertices located on the axis $\theta = 0°$ (points marked as v_1 and v_2 on Fig. 3b). The position of v_2 is given by the mismatch of the lattice parameters between the two layers, which in our case of a MoSe$_2$/ WSe$_2$ heterostructure, is $\epsilon_u = 0.4\%$. The position of v_1 is weighted by ν_{WSe_2}, as the deformation on the armchair axis is 19% of that of the zigzag axis. Now, the vertex is located at $-0.4/0.19 \simeq -2.1\%$. It can easily be seen that a vanishing Poisson ratio can eliminate the divergence of the lattice parameters and lattice area in the negative semi-space. Further information about the effect of the Poisson ratio on the moiré lattice can be found in Supplementary Note 7.

Further insight into how uniaxial strain can affect the moiré lattice geometry can be observed in Fig. 4a, b. Figure 4a shows α (upper panels) and M (lower panels) as function of ϵ_u and θ for
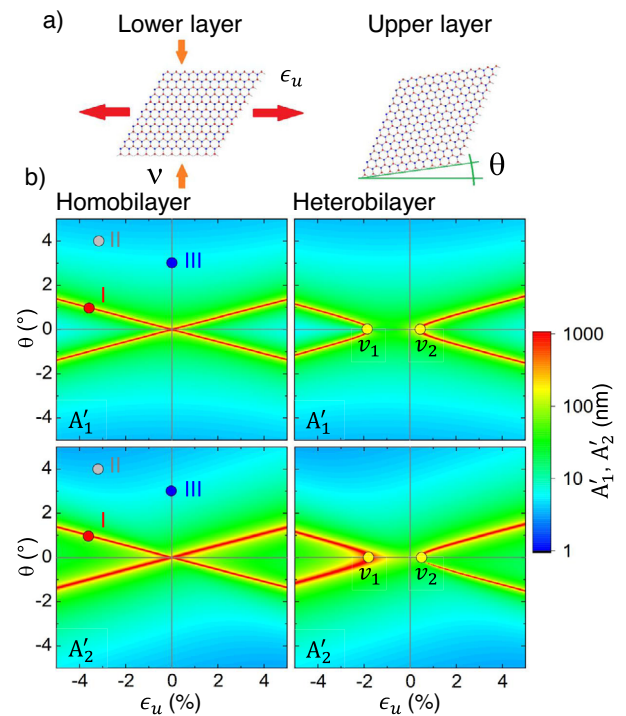

Fig. 3 Deformation of the moiré lattice parameters in hexagonal bilayers under uniaxial heterostrain. a Schematic of moiré lattice formation under uniaxial heterostrain ϵ_u. The deformation of the lower layer due to strain along a zigzag direction and Poisson ratio ν are depicted by the arrows. The upper layer was stacked with an angle θ respect to the lower layer. **b** Moiré lattice parameters A'_1 (upper panels) and A'_2 (lower panels) for the homobilayer- and heterobilayer structures (left and right panels, respectively) as a function of uniaxial strain and stacking angle. Spots labeled as I, II, and III correspond to the different moiré lattices presented in real space in Fig. 4b and those marked as v_1 and v_2 identify the vertexes of the divergence curves in the heterobilayer case.

homo- and heterobilayers. α is a measure of the strong geometrical deformation of the moiré lattice. For instance, by combining θ and ϵ_u, it is possible to generate a rectangular lattice ($\alpha = 90°$), identified by gray dotted lines. On the other hand, for a 1D moiré lattice, indicated by diverging moiré lattice parameters (red lines in Fig. 3b), $\mathbf{A'_1}$ and $\mathbf{A'_2}$ tend to be collinear, i.e., $\alpha \to 0°$ or $\alpha \to 180°$. Note that the divergence of A'_1 and A'_2 also causes a divergence of the moiré unit cell area, even though these lattice vectors tend to be collinear. Figure 4b depicts real space images of some of the accessible moiré lattices by combining ϵ_u and θ. The different geometries correspond to the three points marked as I, II, and III in Figs. 3b and 4a. Point I describes a 1D moiré lattice, point II a rectangular geometry, and III a hexagonal arrangement.

Shear heterostrain on hexagonal homo- and heterobilayers

We finish our discussion on the effect of heterostrain on moiré lattices by presenting the case of shear strain (ϵ_s), once again employing the same material parameters as in previous sections. In Fig. 5a, we sketch the different layers and their deformation/ rotation under the influence of ϵ_s. The case presented corresponds to a sideways load applied along the zigzag direction on the lower layer (violet arrows) while the upper layer is stacked at an angle θ. For simplicity, we will focus our analysis on α and M, shown in Fig. 5b for homobilayer (left) and heterobilayer structures (right). As in the case of uniaxial strain, the moiré lattice parameters and the moiré area diverge along curves in the $\theta - \epsilon_s$ space (red lines). Once again, such divergence is accompanied by the formation of
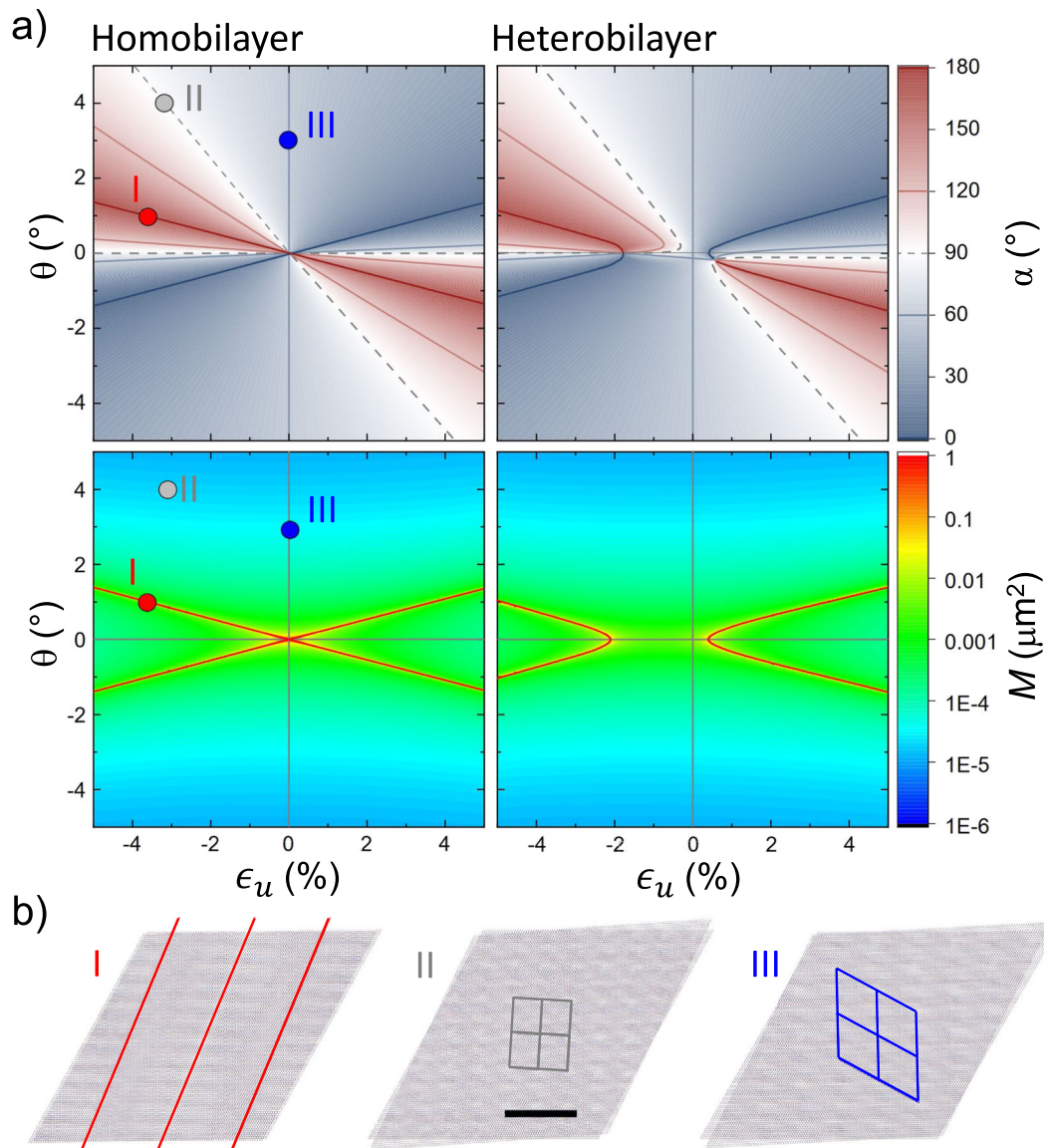
Fig. 4 Effects of uniaxial heterostrain on the geometry and size of moiré lattices formed from hexagonal bilayers. a Relative angle α (upper panels) and moiré lattice area M (lower panels) as function of ϵ_u and θ for the homobilayer (left panels) and heterobilayer structure (right panels). Gray dotted lines denote configurations in which the moiré lattice is rectangular ($\alpha = 90°$). The spots labeled as I, II, and III correspond to the moiré lattices presented in panel **b**. **b** Illustration of moiré lattices corresponding to the points labeled as I, II, and III in panel **a** and in Fig. 3b. The scale bar in II has a length of 30 nm and is valid for all real space moiré patterns I–III. Case I shows a 1D moiré lattice, II a rectangular one, and III a hexagonal one.

1D moiré lattices, as the internal angle α tends to 0° or 180°. Again, the main difference between homo- and heterobilayers is in the vicinity of zero strain and $\theta = 0$, where for heterostructures, the divergence curves do not cross (see red lines in the moiré lattice area). The positions of the vertexes of the curves are located at ±0.4%, since this strain is necessary to fulfill the mismatch between the lattice parameters of the TMDs. As a confirmation of the universality of our mathematical description of moiré lattices, we show similar behavior for moiré patterns formed by rectangular unit cells, such as a homobilayer of WTe_2 in Supplementary Note 8.

In summary, we have presented a general geometrical description of the effect of strain in homo- and heterobilayer systems. We show that heterostrain can be used to form a vast variety of moiré lattice geometries, independent of the underlying lattice size and shape. We demonstrate how an initial moiré lattice geometry can be tuned into a variety of particular moiré patterns, e.g., a hexagonal lattice can be made rectangular or even 1D.

Outlook

Our results are experimentally feasible and can be realized with state-of-the-art strain tuning setups[60–62] (see the Supplementary Material for further details). Although heterostrain is beginning to be explored experimentally[17,63], most strain-tuning experiments focus on homo-strain. However, most existing homostrain setups can also achieve heterostrain by clamping one layer to the substrate while leaving the other one mechanically decoupled from the substrate[64,65]. A thorough presentation of the different experimental setups and clamping configurations is given in Supplementary Note 5, where we also display how to apply pure biaxial, uniaxial, or shear strain as well as their possible combinations.

To verify the influence of strain on the moiré superlattice in a physical experiment, we propose the use of piezo response force
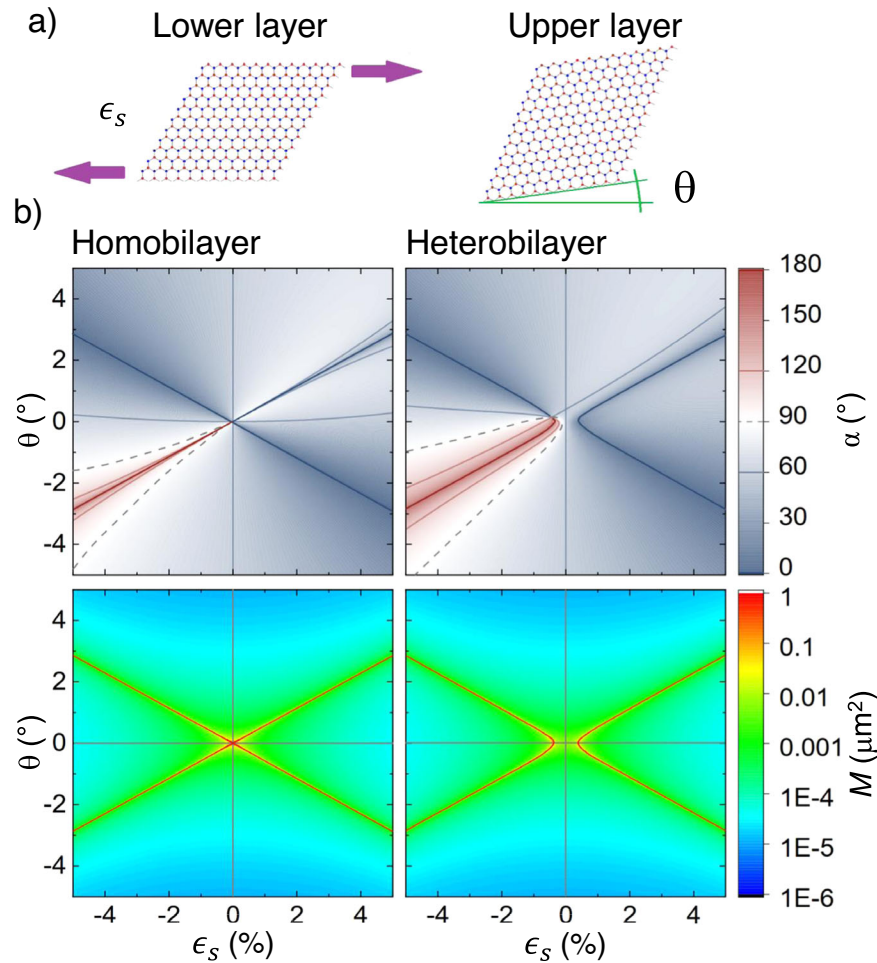
Fig. 5 Moiré lattice deformation in hexagonal bilayers under shear heterostrain. a Scheme of the moiré lattice formation under shear heterostrain ϵ_s. The deformation of the lower layer due to shear strain along the zigzag direction is depicted through arrows. The upper layer was stacked with an angle θ respect to the lower one. **b** Relative angle α (upper panels) and moiré lattice area M (lower panels) as a function of shear strain ϵ_s and stacking angle θ for homobilayer (left panels) and heterobilayer (right panels) systems. Gray dotted lines denote configurations in which the moiré lattice is rectangular ($\alpha = 90°$).

microscopy, which measures polarizations arising due to strain gradients in the moiré[52,66]. The method is very well established and allows the local visualization of the moiré lattice for a variety of different 2D heterostructures. Since piezo response force microscopy only measures the local moiré geometry, it is an ideal tool to verify the deformation of the moiré pattern under strain, as proposed in this paper. The information gained about the size and shape of the moiré at different strain levels can then be used to explain electronic and optical observables, like the change in the photoluminescence emission of moiré excitons from circular polarization in a hexagonal moiré to linear polarization in a 1D moiré pattern[35,52] or the change in carrier density for strongly correlated states in the fractional filling of the moiré lattice[5–11].

The combination of shear and biaxial strains can become powerful knobs to modify, on demand, the moiré pattern size and shape. For example, Fig. 6 presents the combined effect of biaxial and shear strain in a generic hexagonal homobilayer stacked with $\theta = 1°$. From the condition $\epsilon_c = \epsilon_s = 0$, it is possible to change U/t, in situ, by tuning the size of the moiré pattern through biaxial strain (point $\epsilon_c = \epsilon_s = 0$ to point III or to point IV). On the other hand, light green lines in the plot depict the condition $A'_1 = A'_2$. Varying the shear strain along the line that connects point I with II modifies the ratio A'_1/A'_2 which realizes a triangular Hubbard model with two tunable hopping parameters t_1 and t_2. Finally, the point labeled as V in Fig. 6

presents a lattice in which the effect described in $\epsilon_c = \epsilon_s = 0$ can be equivalently applied to a perfect square lattice. The fact that all these moiré patterns are accessible within one experiment highlights the potential of this novel approach. Moiré straintronics offers a powerful new avenue to explore highly correlated quantum systems. As commonly known, once the sample is fabricated, it is usually not possible to tune the stacking angle. Furthermore, achieving precise rotational alignment within the necessary accuracy required near critical points, such as in magic-angle graphene, is very challenging with state-of-the-art fabrication procedures[41]. In contrast to twist angle tuning[29], strain can be applied much more precisely with an accuracy corresponding to 0.0001° in the twist angle (as shown in Supplementary Note 5). In ref. [67], it is shown that flat bands in twisted bilayer graphene can be achieved at an angle of 1.25° when a compressive shear strain of 0.36% is applied to a single layer. Hence, the twist angle set during the fabrication can provide a rough alignment knob, while heterostrain can be used to fine-tune the moiré lattice. Furthermore, heterostrain offers an additional mechanism to generate flat bands in graphene[31,38,63,67,68] or tune highly correlated moiré quantum materials around critical points in the phase diagram[28]. Especially in twisted bilayer graphene, shear heterostrain not only alters the moiré miniband bandwidth but also lifts the particle-hole symmetry and breaks the valley degeneracy of the system[32,67]. A recent experiment in an ex-situ shear
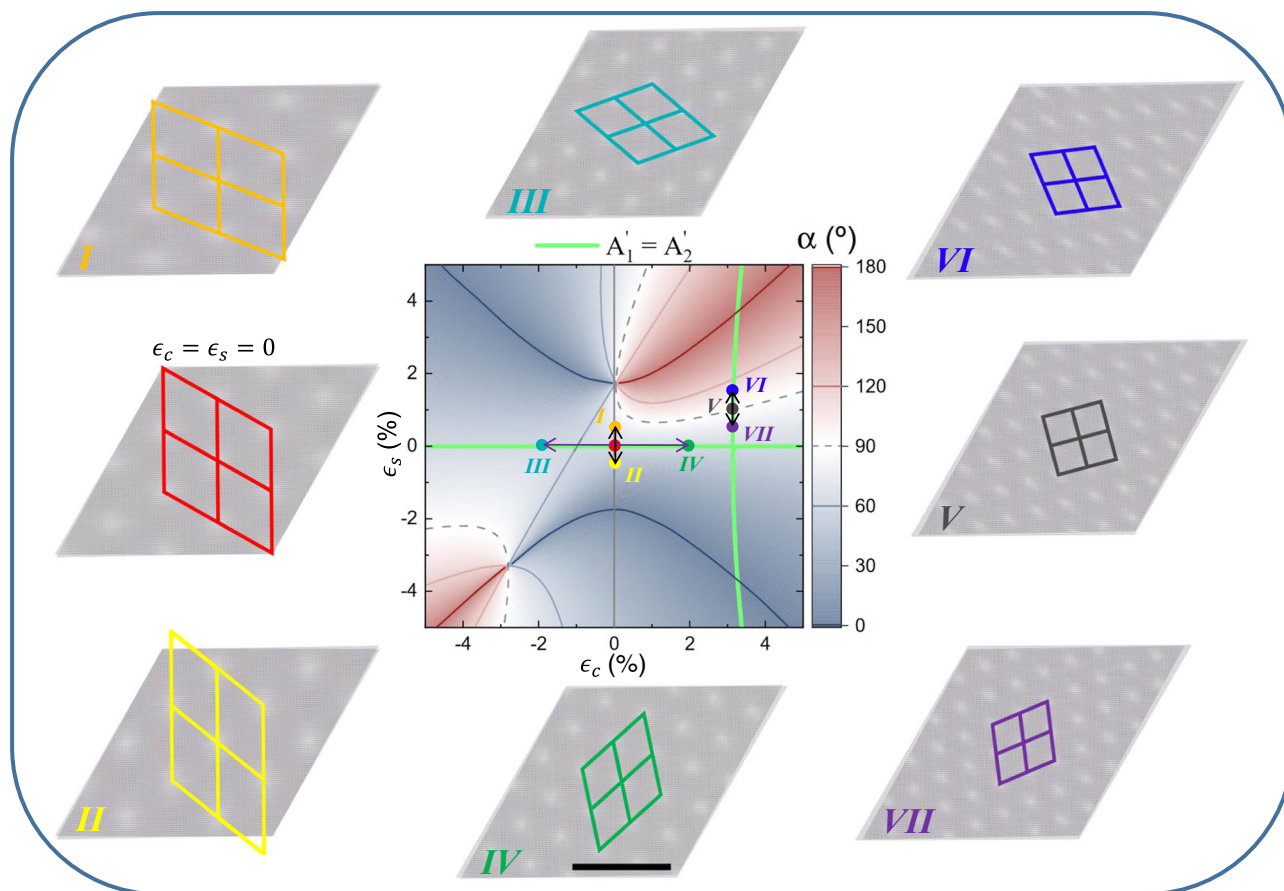
Fig. 6 Geometrical deformation of a general homobilayer stacked at $\theta = 1°$ under biaxial and shear heterostrain. Light green lines denote moiré lattices in which $A_1' = A_2'$. Points labeled as I, II, III, IV, V, VI, and VII correspond to the different illustrations of the moiré pattern in real space. The scale bar in IV has a length of 30 nm in case of a $MoSe_2$ bilayer and is valid for all real space moiré patterns I–VII. An experimental setup for the simultaneous control of biaxial and shear strain is shown in Supplementary Note 5. The computational script to reproduce real space images and strain animations can be found in https://github.com/QuantumPhotonicsLab/Strained-Moire-Visualization.

heterostrained bilayer graphene near the magic angle showed a zero-energy flat band indicating the possibilities of in situ tunable heterostrained systems[67,69].

On the other hand, our mathematical framework presents an important starting point for exploring reconstructed moiré lattices[17–22]. Finally, the capability to in situ tune the geometry and the interaction strength in highly correlated moiré quantum systems is, to the best of our knowledge, unprecedented. We, therefore, expect strain tuning of moiré materials will have a major impact on the exploration of highly interacting quantum systems, from fine-tuning magic-angle graphene to the realization of moiré quantum simulators for Luttinger liquids, the Hubbard model, and beyond.

DATA AVAILABILITY
The data presented were generated from the mathematical algorithm outlined in the main text.

CODE AVAILABILITY
Code for geometrical illustrations of (hetero)strained moiré patterns with the calculated moiré lattice as those presented in Fig. 6 can be found in https://github.com/QuantumPhotonicsLab/Strained-Moire-Visualization.

REFERENCES
1. Kennes, D. M. et al. Moiré heterostructures as a condensed-matter quantum simulator. *Nat. Phys.* **17**, 155–163 (2021).
2. Cao, Y. et al. Unconventional superconductivity in magic-angle graphene superlattices. *Nature* **556**, 43–50 (2018).
3. Cao, Y. et al. Correlated insulator behaviour at half-filling in magic-angle graphene superlattices. *Nature* **556**, 80–84 (2018).
4. Balents, L., Dean, C. R., Efetov, D. K. & Young, A. F. Superconductivity and strong correlations in moiré flat bands. *Nat. Phys.* **16**, 725–733 (2020).
5. Shimazaki, Y. et al. Strongly correlated electrons and hybrid excitons in a moiré heterostructure. *Nature* **580**, 472–477 (2020).
6. Wang, L. et al. Correlated electronic phases in twisted bilayer transition metal dichalcogenides. *Nat. Mater.* **19**, 861–866 (2020).
7. Wang, P. et al. One-dimensional Luttinger liquids in a two-dimensional moiré lattice. *Nature* **605**, 57–62 (2022).
8. Tang, Y. et al. Simulation of Hubbard model physics in WSe2/WS2 moiré superlattices. *Nature* **579**, 353–358 (2020).
9. Regan, E. C. et al. Mott and generalized Wigner crystal states in wse2/ws2 moiré superlattices. *Nature* **579**, 359–363 (2020).
10. Li, T. et al. Quantum anomalous hall effect from intertwined moiré bands. *Nature* **600**, 641–646 (2021).
11. Campbell, A. J. et al. Exciton-polarons in the presence of strongly correlated electronic states in a MoSe2/WSe2 moiré superlattice. *npj 2D Mater. Appl.* **6**, 79 (2022).
12. Seyler, K. L. et al. Signatures of moiré-trapped valley excitons in mose2/wse2 heterobilayers. *Nature* **567**, 66–70 (2019).
13. Baek, H. et al. Highly energy-tunable quantum light from moiré-trapped excitons. *Sci. Adv.* **6**, 1–7 (2020).
14. Song, T. et al. Direct visualization of magnetic domains and moiré magnetism in twisted 2d magnets. *Science* **374**, 1140–1144 (2021).

15. Xie, H. et al. Twist engineering of the two-dimensional magnetism in double bilayer chromium triiodide homostructures. *Nat. Phys.* **18**, 30–36 (2022).

16. Xu, Y. et al. Coexisting ferromagnetic-antiferromagnetic state in twisted bilayer cri3. *Nat. Nanotechnol.* **17**, 143–147 (2022).

17. Edelberg, D., Kumar, H., Shenoy, V., Ochoa, H. & Pasupathy, A. N. Tunable strain soliton networks confine electrons in van der Waals materials. *Nat. Phys.* **16**, 1097–1102 (2020).

18. Hu, G. et al. Topological polaritons and photonic magic angles in twisted α-moo3 bilayers. *Nature* **582**, 209–213 (2020).

19. Chen, M. et al. Configurable phonon polaritons in twisted α-moo3. *Nat. Mater.* **19**, 1307–1311 (2020).

20. Stern, M. V. et al. Interfacial ferroelectricity by van der Waals sliding. *Science* **372**, 1462–1466 (2021).

21. Yasuda, K., Wang, X., Watanabe, K., Taniguchi, T. & Jarillo-Herrero, P. Stacking-engineered ferroelectricity in bilayer boron nitride. *Science* **372**, 1458–1462 (2021).

22. Hao, Z. et al. Electric field-tunable superconductivity in alternating-twist magic-angle trilayer graphene. *Science* **371**, 1133–1138 (2021).

23. Quintanilla, J. & Hooley, C. The strong-correlations puzzle. *Phys. World* **22**, 32 (2009).

24. Jiang, H.-C. & Devereaux, T. P. Superconductivity in the doped Hubbard model and its interplay with next-nearest hopping t. *Science* **365**, 1424–1428 (2019).

25. Tarruell, L. & Sanchez-Palencia, L. Quantum simulation of the Hubbard model with ultracold fermions in optical lattices. *C. R. Phys.* **19**, 365–393 (2018).

26. Gross, C. & Bloch, I. Quantum simulations with ultracold atoms in optical lattices. *Science* **357**, 995–1001 (2017).

27. Wu, F., Lovorn, T., Tutuc, E. & Macdonald, A. H. Hubbard model physics in transition metal dichalcogenide moiré bands. *Phys. Rev. Lett.* **121**, 26402 (2018).

28. Pan, H., Wu, F. & Das Sarma, S. Quantum phase diagram of a Moiré-Hubbard model. *Phys. Rev. B* **102**, 201104 (2020).

29. Ribeiro-Palau, R. et al. Twistable electronics with dynamically rotatable heterostructures. *Science* **361**, 690–693 (2018).

30. Cosma, D. A., Wallbank, J. R., Cheianov, V. & Fal'Ko, V. I. Moiré pattern as a magnifying glass for strain and dislocations in van der Waals heterostructures. *Faraday Discuss.* **173**, 137–143 (2014).

31. Huder, L. et al. Electronic spectrum of twisted graphene layers under heterostrain. *Phys. Rev. Lett.* **120**, 156405 (2018).

32. Bi, Z., Yuan, N. F. & Fu, L. Designing flat bands by strain. *Phys. Rev. B* **100**, 1–9 (2019).

33. Tong, Q. et al. Topological mosaics in moiré superlattices of van der Waals heterobilayers. *Nat. Phys.* **13**, 356–362 (2017).

34. Mannaï, M. & Haddad, S. Twistronics versus straintronics in twisted bilayers of graphene and transition metal dichalcogenides. *Phys. Rev. B* **103**, L201112 (2021).

35. Zheng, H., Zhai, D. & Yao, W. Twist versus heterostrain control of optical properties of moiré exciton minibands. *2D Mater.* **8**, 044016 (2021).

36. Halbertal, D. et al. Moiré metrology of energy landscapes in van der Waals heterostructures. *Nat. Commun.* **12**, 1–8 (2021).

37. Kerelsky, A. et al. Maximized electron interactions at the magic angle in twisted bilayer graphene. *Nature* **572**, 95–100 (2019).

38. Mesple, F. et al. Heterostrain determines flat bands in magic-angle twisted graphene layers. *Phys. Rev. Lett.* **127**, 126405 (2021).

39. Gao, X. et al. Heterostrain-enabled dynamically tunable moiré superlattice in twisted bilayer graphene. *Sci. Rep.* **11**, 1–8 (2021).

40. Georges, A., Giamarchi, T. & Sandler, N. Interchain conductivity of coupled Luttinger liquids and organic conductors. *Phys. Rev. B* **61**, 16393–16396 (2000).

41. Lau, C. N., Bockrath, M. W., Mak, K. F. & Zhang, F. Reproducibility in the fabrication and physics of moiré materials. *Nature* **602**, 41–50 (2022).

42. Kuwabara, M., Clarke, D. R. & Smith, D. Anomalous superperiodicity in scanning tunneling microscope images of graphite. *Appl. Phys. Lett.* **56**, 2396–2398 (1990).

43. Woods, C. R. et al. Commensurate-incommensurate transition in graphene on hexagonal boron nitride. *Nat. Phys.* **10**, 451–456 (2014).

44. Weston, A. et al. Atomic reconstruction in twisted bilayers of transition metal dichalcogenides. *Nat. Nanotechnol.* **15**, 592–597 (2020).

45. Lin, K.-Q. et al. Large-scale mapping of moiré superlattices by hyperspectral Raman imaging. *Adv. Mater.* **33**, 2008333 (2021).

46. Ru, G., Qi, W., Tang, K., Wei, Y. & Xue, T. Interlayer friction and superlubricity in bilayer graphene and MoS2/MoSe2 van der Waals heterostructures. *Tribol. Int.* **151**, 106483 (2020).

47. Song, Y. et al. Robust microscale superlubricity in graphite/hexagonal boron nitride layered heterojunctions. *Nat. Mater.* **17**, 894–899 (2018).

48. Andersen, T. I. et al. Excitons in a reconstructed moiré potential in twisted WSe2/WSe2 homobilayers. *Nat. Mater.* **20**, 480–487 (2021).

49. Enaldiev, V. V., Zólyomi, V., Yelgel, C., Magorrian, S. J. & Fal'ko, V. I. Stacking domains and dislocation networks in marginally twisted bilayers of transition metal dichalcogenides. *Phys. Rev. Lett.* **124**, 1–7 (2020).

50. Wang, K., Ouyang, W., Cao, W., Ma, M. & Zheng, Q. Robust superlubricity by strain engineering. *Nanoscale* **11**, 2186–2193 (2019).

51. Bertolazzi, S., Brivio, J. & Kis, A. Stretching and breaking of ultrathin MoS 2. *ACS Nano* **5**, 9703–9709 (2011).

52. Bai, Y. et al. Excitons in strain-induced one-dimensional moiré potentials at transition metal dichalcogenide heterojunctions. *Nat. Mater.* **19**, 1068–1073 (2020).

53. Yao, K. et al. Enhanced tunable second harmonic generation from twistable interfaces and vertical superlattices in boron nitride homostructures. *Sci. Adv.* **7**, 1–8 (2021).

54. Hu, C. et al. In-situ twistable bilayer graphene. *Sci. Rep.* **12**, 1–8 (2022).

55. Finney, N. R. et al. Tunable crystal symmetry in graphene-boron nitride heterostructures with coexisting moiré superlattices. *Nat. Nanotechnol.* **14**, 1029–1034 (2019).

56. Kang, J., Tongay, S., Zhou, J., Li, J. & Wu, J. Band offsets and heterostructures of two-dimensional semiconductors. *Appl. Phys. Lett.* **102**, 012111 (2013).

57. Project, T. M. Materials data on wse2 by materials project (2020).

58. Schutte, W., De Boer, J. & Jellinek, F. Crystal structures of tungsten disulfide and diselenide. *J. Solid State Chem.* **70**, 207–209 (1987).

59. Yankowitz, M. et al. Emergence of superlattice Dirac points in graphene on hexagonal boron nitride. *Nat. Phys.* **8**, 382–386 (2012).

60. Iff, O. et al. Strain-tunable single photon sources in WSe2 monolayers. *Nano Lett.* **19**, 6931–6936 (2019).

61. Wang, L. et al. Mobility enhancement in graphene by in situ reduction of random strain fluctuations. *Phys. Rev. Lett.* **124**, 1–6 (2020).

62. Hicks, C. W., Barber, M. E., Edkins, S. D., Brodsky, D. O. & Mackenzie, A. P. Piezoelectric-based apparatus for strain tuning. *Rev. Sci. Instrum.* **85**, 065003 (2014).

63. Zhang, L. et al. Correlated states in strained twisted bilayer graphenes away from the magic angle. *Nano Lett.* **22**, 3204–3211 (2022).

64. Wang, L. et al. In situ strain tuning in hBN-encapsulated graphene electronic devices. *Nano Lett.* **19**, 4097–4102 (2019).

65. Liu, Y. et al. Approaching the Schottky-Mott limit in van der Waals metal-semiconductor junctions. *Nature* **557**, 696–700 (2018).

66. McGilly, L. J. et al. Visualization of moiré superlattices. *Nat. Nanotechnol.* **15**, 580–584 (2020).

67. Mannaï, M. & Haddad, S. Twistronics versus straintronics in twisted bilayers of graphene and transition metal dichalcogenides. *Phys. Rev. B* **103**, L201112 (2021).

68. Mesple, F. et al. Heterostrain determines flat bands in magic-angle twisted graphene layers. *Phys. Rev. Lett.* **127**, 126405 (2021).

69. Zhang, Y. et al. Correlation-induced valley splitting and orbital magnetism in a strain-induced zero-energy flatband in twisted bilayer graphene near the magic angle. *Phys. Rev. B* **102**, 081403 (2020).

AUTHOR CONTRIBUTIONS

A.S., M.B.-G., B.G., and J.F. conceived the project. P.S. developed an algorithm for specific strain tunings. M.K. developed the mathematical algorithm for the exact description of a universal Moire strain tuning. P.S. and M.K. interpreted the calculations and wrote the manuscript equally, with contributions from all authors.

COMPETING INTERESTS

The authors declare no competing interests.

ADDITIONAL INFORMATION

Supplementary information The online version contains supplementary material available at https://doi.org/10.1038/s41699-023-00382-4.

Correspondence and requests for materials should be addressed to M. Kögl or P. Soubelet.

Reprints and permission information is available at http://www.nature.com/reprints